



# Improved performance of multi-view fringe projection 3D microscopy

MENG WANG,<sup>1,3</sup> YONGKAI YIN,<sup>2</sup> DINGNAN DENG,<sup>1</sup> XIANGFENG MENG,<sup>2</sup>  
XIAOLI LIU,<sup>1</sup> XIANG PENG<sup>1,\*</sup>

<sup>1</sup>Key Laboratory of Optoelectronic Devices and Systems of Ministry of Education and Guangdong Province, College of Optoelectronic Engineering, Shenzhen University, Shenzhen 518060, China

<sup>2</sup>Shandong Provincial Key Laboratory of Laser Technology and Application, Department of Optics, School of Information Science and Engineering, Shandong University, Jinan 250100, China

<sup>3</sup>wmengszu@outlook.com

\*xpeng@szu.edu.cn

**Abstract:** Fringe projection 3D microscopy (FP-3DM) plays an increasingly important role in micro manufacturing and measurement. In recent decades, research on FP-3DM has made considerable progress. Nevertheless, some disadvantages arising from the limited depth of field, local specular reflection and occlusion still exist and need to be further addressed. In this paper, a multi-view FP-3DM (MVFP-3DM) is presented. Four imaging branches with the Scheimpflug condition and one vertical projection branch are deployed to establish the system. The system is described with a general imaging model, which is independent of the system configuration. In system calibration, the edge of binary fringe is used to locate the benchmark, which takes advantage of the fact that the edge will keep its position whether it is in focus or out of focus. Furthermore, a group of experiments prove that our proposed MVFP-3DM system can extend measurable range in depth, improve precision in 3D reconstruction and reduce occlusion.

©2017 Optical Society of America

**OCIS codes:** (180.6900) Three-dimensional microscopy; (110.1758) Computational imaging; (150.1488) Calibration; (120.5050) Phase measurement; (150.6910) Three-dimensional sensing; (120.6650) Surface measurements, figure.

## References and links

1. J. C. Wyant, C. L. Koliopoulos, B. Bhushan, and O. E. George, "An Optical Profilometer for Surface Characterization of Magnetic Media," *ASLE Trans.* **27**(2), 101–113 (1984).
2. P. J. Caber, "Interferometric profiler for rough surfaces," *Appl. Opt.* **32**(19), 3438–3441 (1993).
3. M. K. Kim, "Principles and techniques of digital holographic microscopy," *PHOTOE*, 018005–018050 (2010).
4. K. Leonhardt, U. Droste, and H. J. Tiziani, "Microshape and rough-surface analysis by fringe projection," *Appl. Opt.* **33**(31), 7477–7488 (1994).
5. M. Khokhlov, A. Fischer, and D. Rittel, "Multi-Scale Stereo-Photogrammetry System for Fractographic Analysis Using Scanning Electron Microscopy," *Exp. Mech.* **52**(8), 975–991 (2012).
6. R. Leach, *Optical Measurement of Surface Topography* (Springer-Verlag Berlin Heidelberg, 2011).
7. Y. Yin, M. Wang, B. Z. Gao, X. Liu, and X. Peng, "Fringe projection 3D microscopy with the general imaging model," *Opt. Express* **23**(5), 6846–6857 (2015).
8. R. Windecker, M. Fleischer, and H. J. Tiziani, "Three-dimensional topometry with stereo microscopes," *Opt. Eng.* **36**(12), 3372–3377 (1997).
9. C. Zhang, P. S. Huang, and F.-P. Chiang, "Microscopic phase-shifting profilometry based on digital micromirror device technology," *Appl. Opt.* **41**(28), 5896–5904 (2002).
10. K. P. Proll, J. M. Nivet, K. Körner, and H. J. Tiziani, "Microscopic three-dimensional topometry with ferroelectric liquid-crystal-on-silicon displays," *Appl. Opt.* **42**(10), 1773–1778 (2003).
11. A. Li, X. Peng, Y. Yin, X. Liu, Q. Zhao, K. Körner, and W. Osten, "Fringe projection based quantitative 3D microscopy," *Optik - International Journal for Light and Electron Optics* **124**(21), 5052–5056 (2013).
12. Y. Q. Yu, S. J. Huang, Z. H. Zhang, F. Gao, and X. Q. Jiang, "The research of 3D small-field imaging system based on fringe projection technique," *International Symposium on Optoelectronic Technology and Application 2014: Laser and Optical Measurement Technology, and Fiber Optic Sensors* **9297**, 8 (2014).
13. C. Quan, X. Y. He, C. F. Wang, C. J. Tay, and H. M. Shang, "Shape measurement of small objects using LCD fringe projection with phase shifting," *Opt. Commun.* **189**(1-3), 21–29 (2001).

14. C. Quan, C. J. Tay, X. Y. He, X. Kang, and H. M. Shang, "Microscopic surface contouring by fringe projection method," *Opt. Laser Technol.* **34**(7), 547–552 (2002).
15. J. Chen, T. Guo, L. Wang, Z. Wu, X. Fu, and X. Hu, "Microscopic fringe projection system and measuring method," in (2013), 87594U–87594U–87599.
16. Q. Mei, J. Gao, H. Lin, Y. Chen, H. Yunbo, W. Wang, G. Zhang, and X. Chen, "Structure light telecentric stereoscopic vision 3D measurement system based on Scheimpflug condition," *Opt. Lasers Eng.* **86**, 83–91 (2016).
17. T. N. Nguyen, J. M. Huntley, R. L. Burguete, and C. R. Coggrave, "Multiple-view Shape and Deformation Measurement by Combining Fringe Projection and Digital Image Correlation," *Strain* **48**(3), 256–266 (2012).
18. M. Weinmann, C. Schwartz, R. Ruiters, and R. Klein, "A Multi-camera, Multi-projector Super-Resolution Framework for Structured Light," in *3D Imaging, Modeling, Processing, Visualization and Transmission (3DIMPVT), 2011 International Conference on*, 2011), 397–404.
19. R. Hartley and A. Zisserman, *Multiple View Geometry in Computer Vision* (Cambridge University, 2003).
20. Z. Chen, H. Liao, and X. Zhang, "Telecentric stereo micro-vision system: Calibration method and experiments," *Opt. Lasers Eng.* **57**, 82–92 (2014).
21. D. Li, C. Liu, and J. Tian, "Telecentric 3D profilometry based on phase-shifting fringe projection," *Opt. Express* **22**(26), 31826–31835 (2014).
22. B. Li and S. Zhang, "Flexible calibration method for microscopic structured light system using telecentric lens," *Opt. Express* **23**(20), 25795–25803 (2015).
23. L. Rao, F. Da, W. Kong, and H. Huang, "Flexible calibration method for telecentric fringe projection profilometry systems," *Opt. Express* **24**(2), 1222–1237 (2016).
24. K. Haskamp, M. Kästner, and E. Reithmeier, "Accurate calibration of a fringe projection system by considering telecentricity," *Proc. SPIE* **8082**, 80821B (2011).
25. O. Albers, A. Poesch, and E. Reithmeier, "Flexible calibration and measurement strategy for a multi-sensor fringe projection unit," *Opt. Express* **23**(23), 29592–29607 (2015).
26. J. Peng, M. Wang, D. Deng, X. Liu, Y. Yin, and X. Peng, "Distortion correction for microscopic fringe projection system with Scheimpflug telecentric lens," *Appl. Opt.* **54**(34), 10055–10062 (2015).
27. T. Bothe, W. Li, M. Schulte, C. von Kopylow, R. B. Bergmann, and W. P. O. Jüptner, "Vision ray calibration for the quantitative geometric description of general imaging and projection optics in metrology," *Appl. Opt.* **49**(30), 5851–5860 (2010).
28. P. Sturm and S. Ramalingam, "A generic concept for camera calibration," *Lect. Notes Comput. Sci.* **3022**, 1–13 (2004).
29. M. D. Grossberg and S. K. Nayar, "A general imaging model and a method for finding its parameters," in *Computer Vision, 2001. ICCV 2001. Proceedings. Eighth IEEE International Conference on*, 2001), 108–115 vol.102.
30. S. Ramalingam, P. Sturm, and S. K. Lodha, "Towards complete generic camera calibration," in *2005 IEEE Computer Society Conference on Computer Vision and Pattern Recognition, CVPR 2005*, in Proceedings of the 2005 IEEE Computer Society Conference on Computer Vision and Pattern Recognition, (CVPR 2005) (Institute of Electrical and Electronics Engineers Computer Society, 2005), 1093–1098.
31. H. Ha, Y. Bok, K. Joo, J. Jung, and I. S. Kweon, "Accurate Camera Calibration Robust to Defocus Using a Smartphone," in *2015 IEEE International Conference on Computer Vision (ICCV)*, 2015), 828–836.

## 1. Introduction

Three-dimensional (3D) shape measurement is an indispensable part of modern manufacturing industry. Especially the 3D shape measurement using optical methods, with the advantages of non-contact, high-speed and full-field, has become more and more important in industrial inspection. Over the past decades, with the well development of precision manufacturing, the demand for 3D shape measurement in a tiny and micro scale is increasing rapidly. Depending on the measurement principle, most optical methods for microscopic 3D shape measurement fall into two categories: interferometry and triangulation. For instance, phase shifting interferometry (PSI) [1], coherence scanning interferometry (CSI) [2] and digital holographic microscopy (DHM) [3], are all working based on interferometry, while fringe projection [4] and stereo photogrammetry [5] belong to triangulation [6]. As the characteristics of coherent measurement, interferometry is competent for the measurement tasks even requiring nanometer resolution. In contrast, triangulation can provide robust measurement with field of view (FOV) from order of  $\text{mm}^2$  to  $\text{cm}^2$  and archive depth resolution in an order of micrometer.

Comparing with confocal microscopy and stereo photogrammetry, fringe projection has advantages of full-field and high data density, thus plays an increasingly important role in precision manufacturing and measurement. The microscopic 3D shape measurement using

fringe projection technique, which is also referred to as fringe projection 3D microscopy (FP-3DM) [7], is normally built with two different frameworks. One is based on the modification of stereo microscopy [8–12], and another employs a long working distance (LWD) lens [7,13–15]. Because LWD lens used for projection and imaging can be selected with different parameters, the latter framework is more flexible in magnification match, working distance adjustment and configuration design [7]. Nevertheless, some disadvantages still exist in current FP-3DM and need to be further addressed. The first one is the limited measurable range in depth. Actually, it is an inherent limitation of all microscopic imaging system due to the limited depth of field (DOF), which is aggravated in FP-3DM due to the requirement of common focus area for both projection and imaging. The second one is the large dynamic range arisen from the local specular reflection of the surface. Fringe projection is a typical directional illumination, which will generate large intensity in the direction of specular reflection. Hence there will be a great number of over-exposure pixels in the captured image, which leads to artifacts of 3D reconstruction in corresponding positions. The third one is occlusion, which is a common problem for 3D shape measurement using fringe projection, whether in micro and tiny scale or macro scale. In this paper, a dedicated FP-3DM system is proposed to address above mentioned problems. The system framework employs multi-view stereo and Scheimpflug condition, and the system is described with the general imaging model and calibrated with planar target. The characters of multi-view stereo are well exploited to improve the performances on 3D shape measurement, which leads to extended measurable range, improved precision and reduced occlusion in 3D reconstruction. The system configuration and calibration are detailed in Section 2. The performances of the system in terms of measurable range, precision and occlusion are presented and analyzed in Section 3. And the conclusion is presented in Section 4.

## 2. System configuration and calibration

### 2.1 System design and configuration

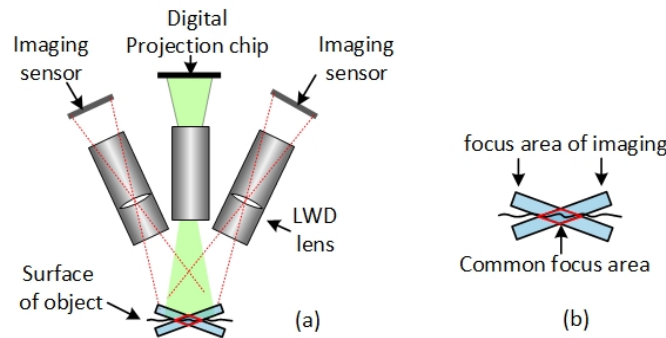


Fig. 1. Fringe projection 3D microscopy (FP-3DM) based on binocular stereo vision. (a) The schematic of setup. (b) The common focus area (Marked with red quadrangle).

Almost all established FP-3DM systems using LWD lens have a simple and similar layout. It consists of a projection branch and an imaging branch with an angle between each other. In the projection branch, the fringe pattern is generated and projected onto the object surface through one LWD lens. In the imaging branch, the deformed fringe pattern reflected from the surface is captured by the camera through another LWD lens. And then the surface topography can be reconstructed with appropriate system model and phase retrieval algorithms. It is well known that the binocular stereo vision with fringe projection has been widely used for 3D shape measurement in macro scale because of its better stability and accuracy. However, the binocular structure is seldom employed in FP-3DM system. Because in micro imaging system, the limited DOF usually results in a flat focus area, as shown in Fig. 1(a). The flat focus area is parallel to the sensor chip, which means there is an angle between

the focus areas of each imaging branch. Therefore, the common focus area of the binocular stereo vision is extremely small, as shown in Fig. 1(b).

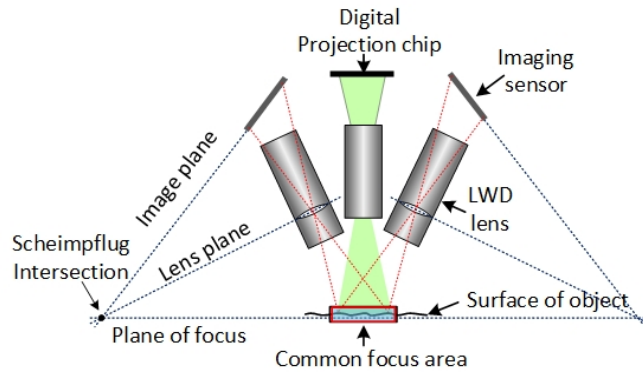


Fig. 2. System design based on the Scheimpflug principle.

To make full use of the limited DOF, a special angle between the sensor and the LWD lens is introduced based on the Scheimpflug principle, which will lead to larger common focus area [7, 16], as shown in Fig. 2. The orientation and position of the sensor chip and LWD lens are carefully fitted so that the sensor plane, the principal plane of the LWD lens, and the object plane make a Scheimpflug intersection. Meanwhile, the projection branch is set perpendicular to the object plane. Therefore, the focus area of different imaging branch and the projection branch can be adjusted to be overlapped to obtain a larger common focus area, where the surface of object can be imaged clearly throughout the whole FOV for each sensor simultaneously. The positive effect of proposed system design is shown in Fig. 3. The image of a planar dot matrix is captured when the optical axis of the LWD lens is not perpendicular to the plane. Due to the limited DOF, it is impossible to obtain a homogeneously sharp image for traditional imaging setup, which can be seen in Fig. 3(a). By contrast, this problem can be solved via modifying the setup with the Scheimpflug condition, as shown in Fig. 3(c). Figure 3(b) and 3(d) are profile line plot of selected points in Fig. 3(a) and 3(c) respectively, which can contrastively show the blurriness of edges.

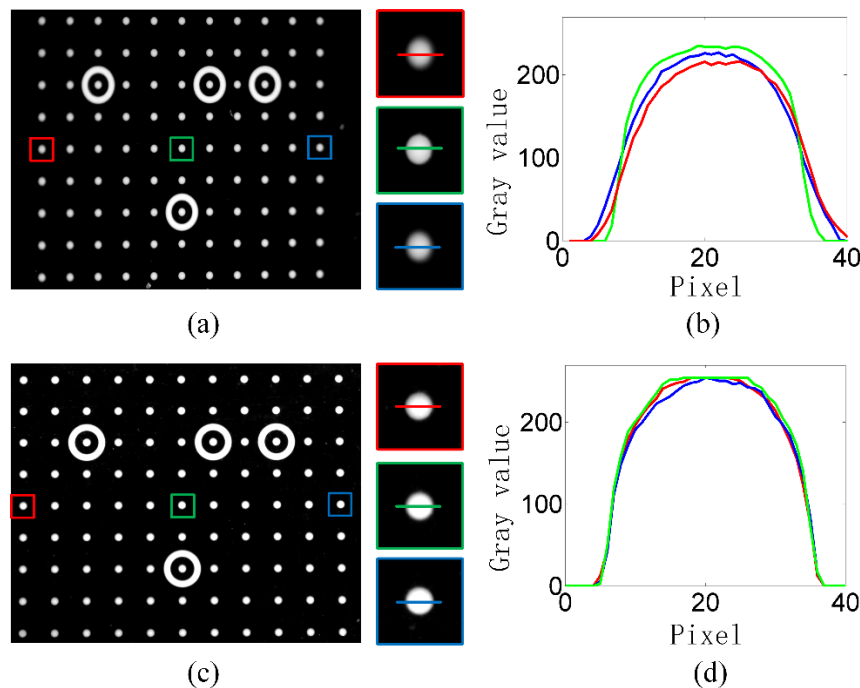


Fig. 3. Captured images of a planar dot matrix when the optical axis of LWD lens is not perpendicular to it. (a) With traditional setup. (b) Profile line plot of selected points in (a). (c) With modified setup considering Scheimpflug condition. (d) Profile line plot of selected points in (c).

Meanwhile four imaging branches are deployed to establish a multi-view FP-3DM system (MVFP-3DM). The usage of multi-view stereo vision framework is based on the following considerations. Firstly, the DOF of FP-3DM limits the measurable range in depth, while the surface to be measured may beyond this range. Multi-view may help to extend the measurable range in depth. Secondly, as a directional illumination manner, the fringe projection makes the object surface to show more specular reflection, and then cause artifacts in 3D reconstruction. Multi-view is a useful method to reduce artifacts in this situation [17]. Thirdly, due to the principle of triangulation, shadow areas lacking meaningful data often appear in the measurement results of FP-3DM system when any occlusion exists in the FOV of camera or projector. Multi-view can effectively reduce shadow areas due to camera occlusion by providing different viewpoints [18].

The layout of proposed MVFP-3DM is shown in Fig. 4(a). The projection branch is perpendicular to the object plane, so the focus area of projection and the surface of object will overlap. The four imaging branches are set around the projection branch, and the Scheimpflug principle is exploited to make the focus areas of imaging overlap with each other and that of the projection. In other words, the focus areas of five channels (imaging and projection) in MVFP-3DM is designed to overlap with each other to obtain the common focus area as large as possible. To verify the proposed design, a prototype of the MVFP-3DM system is established, as shown in Fig. 4(b). A projection module (based on TI 0.45" WXGA DMD, resolution  $1280 \times 800$ ) combined with a LWD lens of  $0.8 \times$  magnification serve as the projection branch, while 4 CMOS cameras (China Daheng (Group) Co., Ltd, MER-130-30UM, resolution  $1280 \times 1024$ ) with LWD lens of  $1 \times$  magnification serve as the imaging branch. Between the camera and LWD lens, a connector with an appropriate wedge angle is used to introduce Scheimpflug condition. Meanwhile, the LWD lens can be rotated slightly to focus. Each imaging branch is mounted on the main platform with a capability of minor

adjustment in three degrees of freedom ( $x$ ,  $y$ , and  $z$ ) to match the FOV and DOF of others. The whole platform is installed on a lifting column for convenient movement in  $z$  direction. Due to the limited fitting space of designed framework, the DMD chip has to be assembled with horizontal rotation of  $45^\circ$ . In order to make the capture fringe in camera keep horizontal and vertical, when the system is working, the standard fringe patterns should also be rotated  $45^\circ$  to match the assembly.

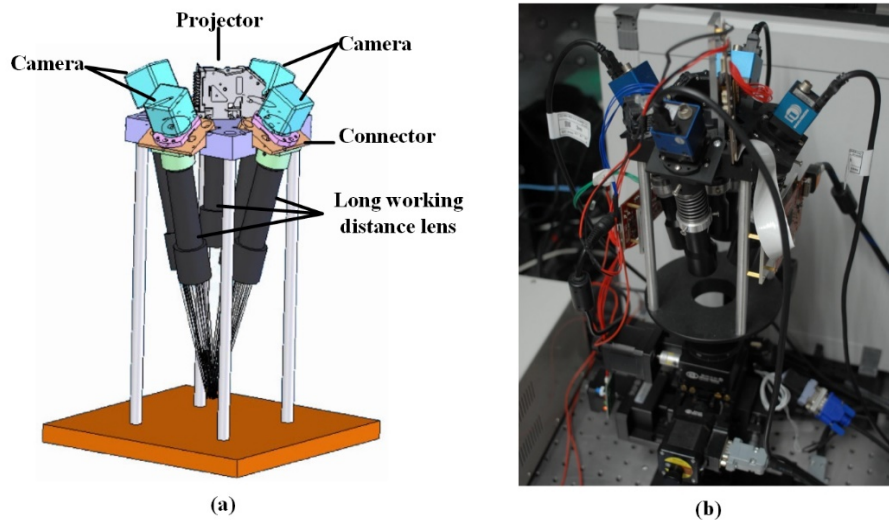


Fig. 4. MVFP-3DM system. (a) The schematic design, (b) The photograph of the system.

## 2.2 System model and calibration

The LWD lens adopted in our MVFP-3DM system is telecentric lens. Because its aperture stop is placed at the image-side focal point, the projection center lies at infinity on the object side. For this property, the telecentric lens does not fit the pinhole camera model any more but should be described with the orthographic projection [19]. Several calibration methods have been proposed according to its special imaging model [20–24]. However, these methods are not suitable for our MVFP-3DM system as its imaging branch has been modified. In addition, another calibration method has been researched for fringe projection system with cameras modified by Scheimpflug condition but non-telecentric lens are used [25]. Recently, two works on calibrating camera with telecentric lens in Scheimpflug condition have been reported [16, 26]. In both methods, besides the standard orthographic projection imaging model, some more parameters are introduced to describe the special imaging system. These parameters are deduced from analyzing the variation of imaging before and after tilting the imaging sensor. It is worth to note that the bi-telecentric lens and object-side telecentric lens are separately adopted in the two methods. The difference of image-side light path (parallel rays and convergent rays) between the two types of telecentric lens means that the two imaging models are not applicable to each other. Otherwise, compared with camera calibration in macro scale, due to the limited DOF in microscopy, it is a more demanding work to obtain a number of sharp images of the planar target with different positions and orientations, which is necessary for the numerical stability of parameter estimation. In this case, we used a simplified calibration method, which is based on a ray-based general imaging model [27–29]. In principle, the general imaging model is applicable to describe all types of imaging system, of course, including the telecentric lens with Scheimpflug condition. And the calibration can be accomplished based on at least three different poses of the planar target [30], which makes the procedure of calibration simple.

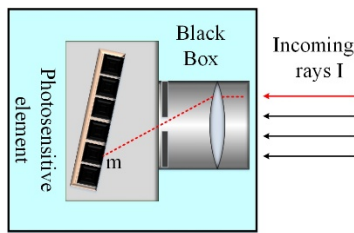


Fig. 5. The ray-based general imaging model

The ray-based general imaging model is introduced based on the geometrical optics, which considers that imaging is the process of collecting incoming rays from scene onto photosensitive element (e.g. CMOS sensor) via imaging system. Therefore, each pixel of the sensor corresponds to a specific pencil of rays. Within the DOF of the imaging system, a pencil of rays can be considered as well focused, thus can be represented with the single chief ray. In this sense, the imaging system can be regarded as a black box. All the variation of imaging system arisen from the orthographic projection, Scheimpflug condition and even distortion of lens could be included in the corresponding relationship between the pixel  $\mathbf{m}$  and the incoming (chief) ray  $\mathbf{I}$ , as shown in Fig. 5. The projection can be regarded as the inverse progress of imaging, thus can also be described with the same model. The 3D range image  $\mathbf{X}$  can be reconstructed by calculating the intersection between the rays from cameras and projector respectively. It is worth emphasizing that the rays must be corresponding to the same point on the surface of object. The related pixels of these rays are usually called homologous point pairs. To search for homologous point pairs, identical label should be assigned to every pixel of all cameras. In fringe projection system, absolute phase values  $\phi^u$  and  $\phi^v$  in horizontal and vertical directions respectively are employed as the identical labels. The absolute phase values can be extracted via popular phase shifting algorithm and phase unwrapping techniques. Pixels on each camera which have the same phase values are taken as homologous point pairs. If  $\mathbf{m}_i$  is an image point of  $\mathbf{X}$  in the  $i$ th camera, the absolute phase values of  $\mathbf{X}$  must be  $(\phi_i^u(\mathbf{m}_i), \phi_i^v(\mathbf{m}_i))$ . By searching absolute phase maps in the  $j$ th camera, if there exist a point  $\mathbf{m}_j$  satisfying the following conditions  $\phi_i^u(\mathbf{m}_i) = \phi_j^u(\mathbf{m}_j)$  and  $\phi_i^v(\mathbf{m}_i) = \phi_j^v(\mathbf{m}_j)$ , the point  $\mathbf{m}_j$  must be the homologous point of  $\mathbf{m}_i$ . Thus the 3D imaging with the MVFP-3DM system can be expressed as follows

$$\begin{cases} \mathbf{m}_p \leftrightarrow I_p, \mathbf{m}_a \leftrightarrow I_a, \mathbf{m}_b \leftrightarrow I_b, \mathbf{m}_c \leftrightarrow I_c, \mathbf{m}_d \leftrightarrow I_d \\ \mathbf{X} = (I_i \wedge I_j), \forall \phi_i^u(\mathbf{m}_i) = \phi_j^u(\mathbf{m}_j) \text{ and } \phi_i^v(\mathbf{m}_i) = \phi_j^v(\mathbf{m}_j), i, j \in \{p, a, b, c, d\} \end{cases} \quad (1)$$

where the subscript  $p$  denotes the projector, and the subscripts  $a, b, c$  and  $d$  denote the four cameras in the MVFP-3DM system respectively. The symbol  $\leftrightarrow$  denotes the implicit correspondence between  $\mathbf{m}$  and  $I$ . This general imaging model can be calibrated using a planar target with known benchmarks and placed in 3 different poses. More details of principle and algorithm can refer to our previous paper [7] about FP-3DM system, here just the process of the benchmark and the result of calibration are discussed as follows.

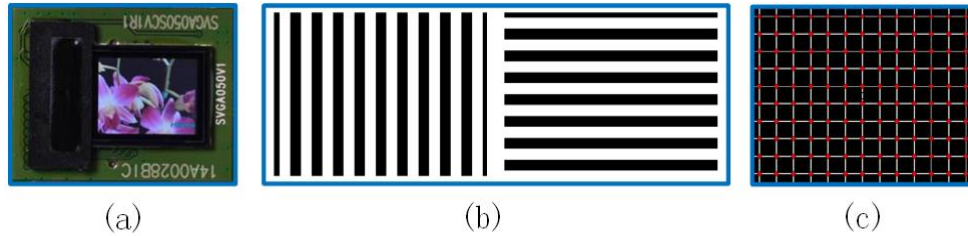


Fig. 6. The calibration target and benchmarks. (a) The micro OLED display chip, (b) The orthogonal binary fringe patterns, (c) The benchmarks (red dots) and edges (white line).

To match the small FOV of MVFP-3DM system, a micro Organic Light-Emitting Diode (OLED) display chip is employed as the calibration target, which is shown in Fig. 6(a). Its size is  $10.13 \times 7.61 \text{ mm}^2$  and pixel resolution is  $800 \times 600$ , which means it can provide enough pixel features within the small FOV. Meanwhile, as a display device, the OLED chip can display a series of designed patterns without mechanical movement. Orthogonal binary fringe patterns, as shown in Fig. 6(b), are consecutively displayed on the OLED chip. Edges of the binary patterns can be extracted from the captured images and the intersection points of orthogonal edges are selected as benchmarks. As shown in Fig. 1(c), the white line is the edge of binary fringe, and the red dot is the benchmark. The edge of binary fringe is used to locate the benchmark, which takes the advantage of that the edge will keep its position whether the chip is in focus or out of focus. For system calibration, the coordinates of benchmark in two coordinate systems are needed, including pixel coordinates on the image and 3D coordinates on the OLED chip.

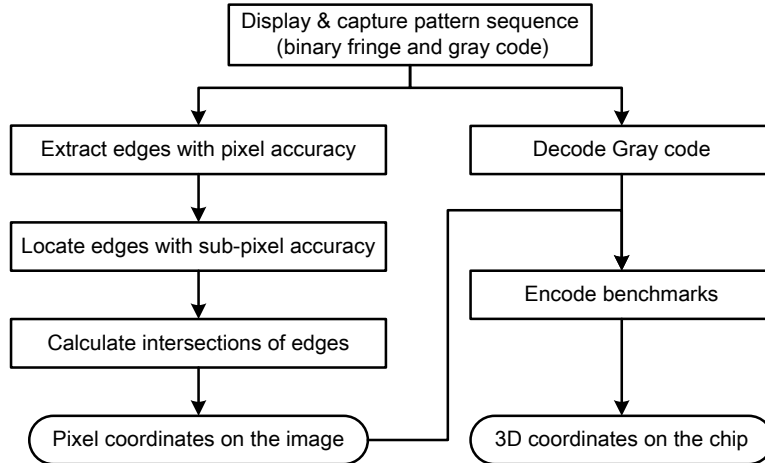


Fig. 7. The process of extracting benchmarks.

Figure 7 schematically shows the process of extracting benchmarks for calibration. Considering the smoothness of the edge arising from the limited aperture and out of focus, complementary binary fringes [31] are introduced to realize robust edge detection. Here we select the vertical binary fringe patterns for illustration.  $I$  and  $I_C$  are the images of a pair of complementary binary fringes, as shown in Fig. 8(a). The initial edges with pixel accuracy can be located via the following equation:

$$\text{Edge}(x, y) = |I(x, y) - I_C(x, y)| < \alpha(I_{\max} - I_{\min}) \quad (2)$$

where  $\alpha$  is a coefficient less than 1,  $I_{\max}$  and  $I_{\min}$  are the maximum and minimum gray values respectively. Figure 8(b) shows the curves of the gray value corresponding to the same

position in images  $I$  and  $I_C$ . The blue and red curves are corresponding to  $I$  and  $I_C$ , respectively. And the position is marked using line segment with corresponding color in Fig. 8(a). It is easy to see that the absolute value of  $|I(x, y) - I_C(x, y)|$  will decrease near the edges of binary fringe, where the region is illustrated with green color in Fig. 8(b). Therefore, the edge can be roughly located with Eq. (2). Here  $\alpha$  is set to 0.8 empirically. After that, a simple morphological erosion is executed to extract the skeleton of the edge. The result is shown in Fig. 8(c). Furthermore, the expressions of the two curves near the initial edges (within the green region) can be fitted with the gray values of the neighborhood. And then the edge can be located with sub-pixel accuracy by calculating the intersection of the two curves. After that, the pixel coordinates of benchmarks can be calculated with the intersection of two orthogonal edges.

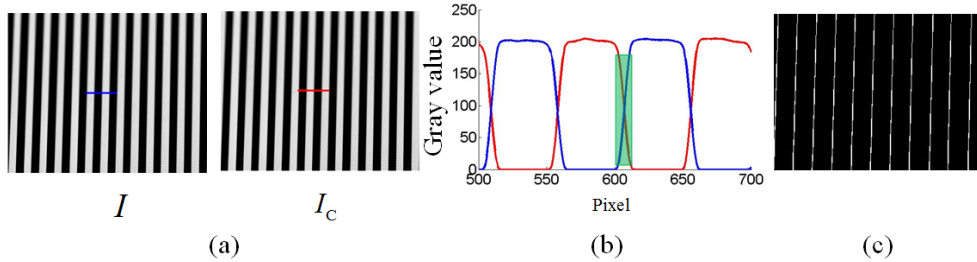


Fig. 8. Edge extraction from complementary binary fringes. (a) Complementary binary fringes, (b) Curves of the gray value, (c) Extracted skeleton of the edge.

Besides the pixel coordinates on the captured image, the 3D coordinates of the same benchmark on the OLED chip are also need. As the benchmark is determined with designed patterns and the pixel size of the OLED chip is known, 3D coordinates of every benchmark on the OLED chip are known. The unknown information is that a benchmark on the image relates to which 3D coordinates on the chip. Here the Gray code is employed to encode the benchmark, with designed horizontal and vertical Gray code, each known 3D coordinates of the benchmark corresponds to a known code value. A series of horizontal and vertical Gray code patterns are displayed and captured, from which the code value map on the image is decoded. With the assistant of the pixel coordinates, each benchmark can be given an exclusive code value, with which the 3D coordinates of this benchmark on the chip can be determined.

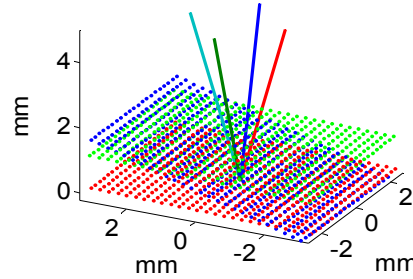


Fig. 9. Calibration result. The three sets of points with different colors show the 3D position of benchmarks related to three different target poses, and the four lines indicate one of the rays corresponding to the four imaging branches respectively.

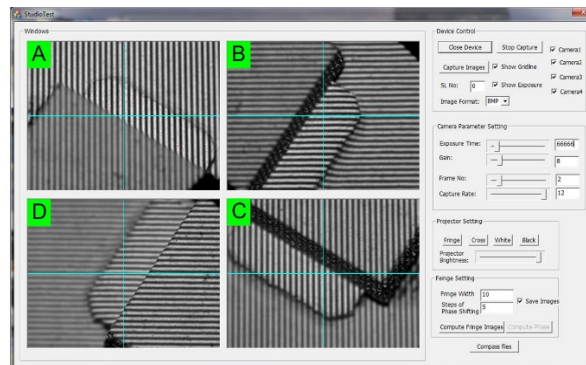
Finally, the system can be calibrated with plenty of benchmarks as well as their pixel coordinates and 3D coordinates [7]. The result of calibration is schematically shown in Fig. 9, where the three sets of points with different colors show the 3D position of benchmarks

related to three different target poses, and the four lines indicate one of the rays corresponding to the four imaging branches respectively.

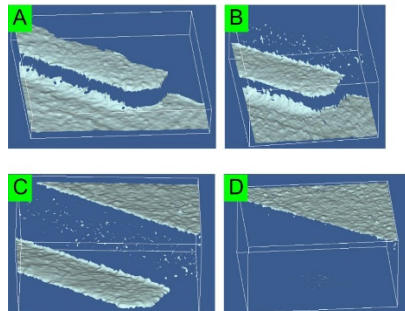
### 3. Improved performance in 3D shape measurement

#### 3.1 Extended measurable range in depth

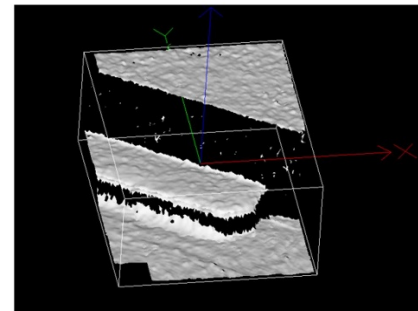
In general, microscopic imaging has limited DOF, therefore the single FP-3DM branch (one camera-projector pair) has limited measurable range in depth as well. If the height of specimen is out of the measurable range, multiple measurements with different focal positions along the z-axis are needed to cover the full depth range of the specimen. However, if we adjust the four FP-3DM branches of the MVFP-3DM system to make them have in turn raised focal positions and overlap measurable range one by one, the MVFP-3DM system will have extended measurable range in depth.



(a)



(b)



(c)

Fig. 10. The experimental results for the specimen with two steps. Each FP-3DM branch (marked with A, B, C and D respectively) has different focal positions. (a) The capture interface of the MVFP-3DM system. (b) The range image from each FP-3DM branch. (c) The integrated range image.

We use a specimen with two steps to test the system, as shown in Fig. 10. The measurable range of each FP-3DM branch is about 1mm and the height of the two steps are 0.68mm and 2.57mm. Figure 10(a) is the capture interface of the system, it can be seen that none of the FP-3DM branch can capture sharp fringe throughout the surface of the specimen, which means the height of the whole specimen exceeds the measuring range of single FP-3DM branch. Moreover, it can also be seen that the branch A has sharp fringe at the bottom, the branch B and C have sharp fringe on the middle step, and the branch D has sharp fringe on the top. Figure 10(b) is the measured range image from each FP-3DM branch. None of the FP-3DM branch can get the data of top and bottom simultaneously, which is the subsequent

result of Fig. 10(a). However, the integrated range image in Fig. 10(c) covers the full height of the specimen, which indicates that the MVFP-3DM system has extended measuring range in depth when the four FP-3DM branches have in turn raised focal positions.

To evaluate the measurable range of the system, the contrast of binary fringe in different depths is calculated. The OLED chip displayed binary fringe is placed parallel to the  $x$ - $o$ - $y$  plane (perpendicular to the optical axis of the projection branch), and then translated 27 times along the direction of  $z$ -axis. The translation distance between adjacent positions is 100 $\mu$ m. When the binary fringe is out of focus, its contrast will decrease rapidly. The contrast curves of each camera are shown in Fig. 11, where the red line indicates the half of the maximum contrast. If the full width at half maximum (FWHM) of the contrast curve is taken as the measurable range, it can be seen that the measurable range of single FP-3DM branch is about 1mm, while that of the MVFP-3DM system closes to 2.5mm, which is consistent with the performance of the previous experiment. It is also worth to point out that if the system allows bigger contrast variation, which means the overlap of contrast curves can be further reduced, this system can extend the measurable range more by further separating the focal positions of each branch.

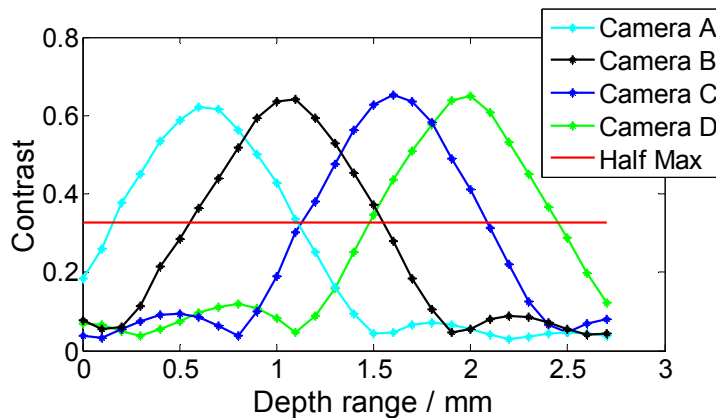


Fig. 11. Contrast curves of the system. The red line indicates the half of the maximum contrast.

### 3.2 Improved precision in 3D reconstruction

From Eq. (1), it can be seen that the precision of 3D reconstruction largely depends on the accuracy of correspondence searching, which is determined by the absolute phase map. Fringe projection is a typical directional illumination, which will generate large intensity in the direction of specular reflection. Hence there will be a great number of over-exposure pixels in the captured image, which leads to artifacts in the absolute phase map. It means there will be inevitable errors when searching the homologous point pairs with inaccurate phase, which leads to low precision in subsequent 3D reconstruction. However, since each imaging branch of the system can provide a ray related to the same 3D point, with the addition of the ray from projection branch, five rays can participate in the 3D reconstruction, as expressed in Eq. (1). In this case, 3D reconstruction for MVFP-3DM system can derive from the intersection of five rays. While for single FP-3DM branch or traditional FP-3DM system, its 3D reconstruction only derives from the intersection of two rays. In fact, due to errors of system parameters and phase information, even two rays almost impossible intersect into the same point. Two rays in 3D coordinate system can provide 4 constraints (each additional ray provides 2 extra constraints), which leads to overdetermined equations for 3 coordinates of the 3D point. Actual 3D reconstruction is just estimating the least square solution of 3D coordinates with the overdetermined equations from at least two rays. On the other hand, the phase quality of the fringes captured by these four cameras is different from each other, which means the reliabilities of the four rays from four cameras should not be

equal. With consideration of the error synthesis theory, different weights should be assigned to equations of different rays respectively according to their reliabilities. Here the modulation index of the fringe is employed as the weight factor. And 3D reconstruction is just estimating the weighted least square solution of equations. Figure 12 comparatively shows the 3D reconstruction for the surface of a coin with different number of lines. The surface of a coin marked with red rectangle in Fig. 12(a) is measured with proposed MVFP-3DM system. The results of 3D reconstruction derived from the intersection of 2-5 rays are shown in Fig. 12(b)-12(e) respectively. To evaluate the precision of 3D reconstruction quantitatively, parts of the 3D surface marked with red rectangles in Fig. 12(b)-12(e) are fitted with plane and the distributions of fitting errors are shown in Fig. 12(f)-12(i) respectively. The standard deviations (Std.) of the fitting errors are also listed in Table 1. It can be clearly seen that proposed MVFP-3DM system can provide improved precision in 3D reconstruction.

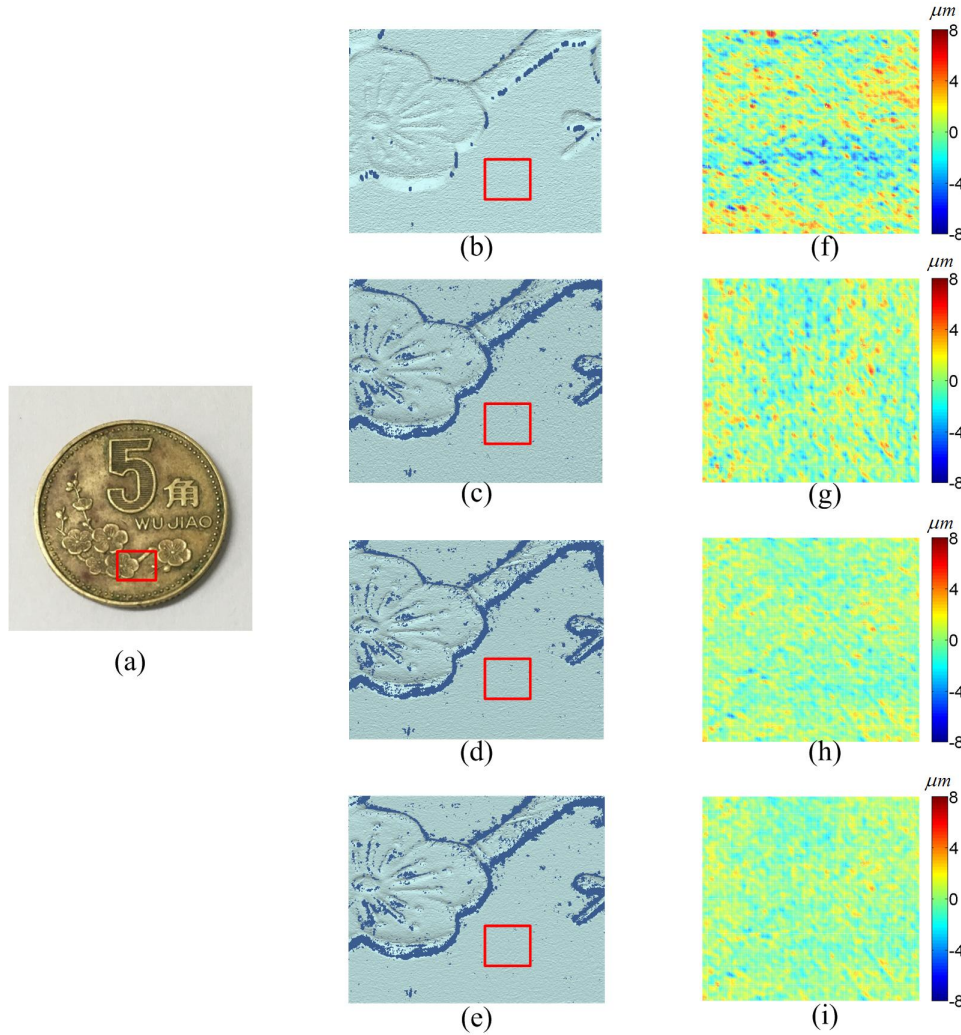


Fig. 12. Comparative results of 3D reconstruction for the surface of a coin. (a) The coin. (b)-(e) The results of 3D reconstruction derived from the intersection of 2-5 rays respectively. (d)-(i) Fitting error distributions of selected areas from (b)-(e) respectively.

**Table 1. Standard deviation (Std.) of the fitting errors**

Number of rays participating in the 3D reconstruction	2	3	4	5
Std. of the fitting errors (Unit: $\mu\text{m}$ )	1.83	1.38	1.02	0.95

To evaluate the accuracy of 3D reconstruction with our method, the OLED display chip is first placed parallel to the  $x$ - $o$ - $y$  plane and then translated 5 times along the direction of  $z$ -axis with a motorized stage. The translation distance between adjacent positions is  $100\mu\text{m}$ , which is treated as the gauge length. On each position, the 3D range image of surface of the OLED display chip is reconstructed with calibrated MVFP-3DM system. 9 points within the FOV of the system are randomly selected. For each selected point, plane fitting is applied to its neighborhood in all the range images, then the translation distance can be calculated with fitted plane parameters. Measurement results of 5 translation distances on the 9 selected points are shown in Table 2. It can be seen the standard deviation (Std.) of distance measurement is less than  $0.6\mu\text{m}$ . While the mean value (Mean) of distance measurement has relatively large variation, which may partly due to the translation error of the motorized stage (without closed-loop control).

**Table 2. Measured translation distance on selected points**

Measured translation distance ( $\mu\text{m}$ )									Statistic ( $\mu\text{m}$ )	
									Mean	Std.
98.1	98.7	98.4	98.9	99.5	98.2	98.1	98.7	97.7	98.5	0.53
106.7	105.9	106.1	106.0	106.6	106.8	106.9	106.6	106.0	106.4	0.42
97.3	97.7	97.0	97.3	97.2	97.5	96.3	97.1	97.7	97.2	0.44
102.1	102.8	101.7	101.9	102.5	102.2	101.8	102.3	102.6	102.2	0.38
102.4	102.7	102.5	102.0	103.0	102.8	101.8	101.8	103.4	102.5	0.55

### 3.3 Reduced occlusion

The MVFP-3DM essentially belongs to triangulation based 3D measurement, which means that a measurable point for the system must be visible for one of the cameras and the projector. Any occlusion in the FOV, either for the camera or the projector, will lead to a related shadow area lacking meaningful data, as shown in Fig. 13(a), 13(c) and 13(e). Fortunately, the occlusion in one viewpoint may be visible in another viewpoint, range images from different viewpoints are naturally complementary. Therefore, the MVFP-3DM system, which combines four FP-3DM branches with different viewpoints, will effectively reduce the missing area due to occlusion, as shown in Fig. 13(b), 13(d) and 13(f).

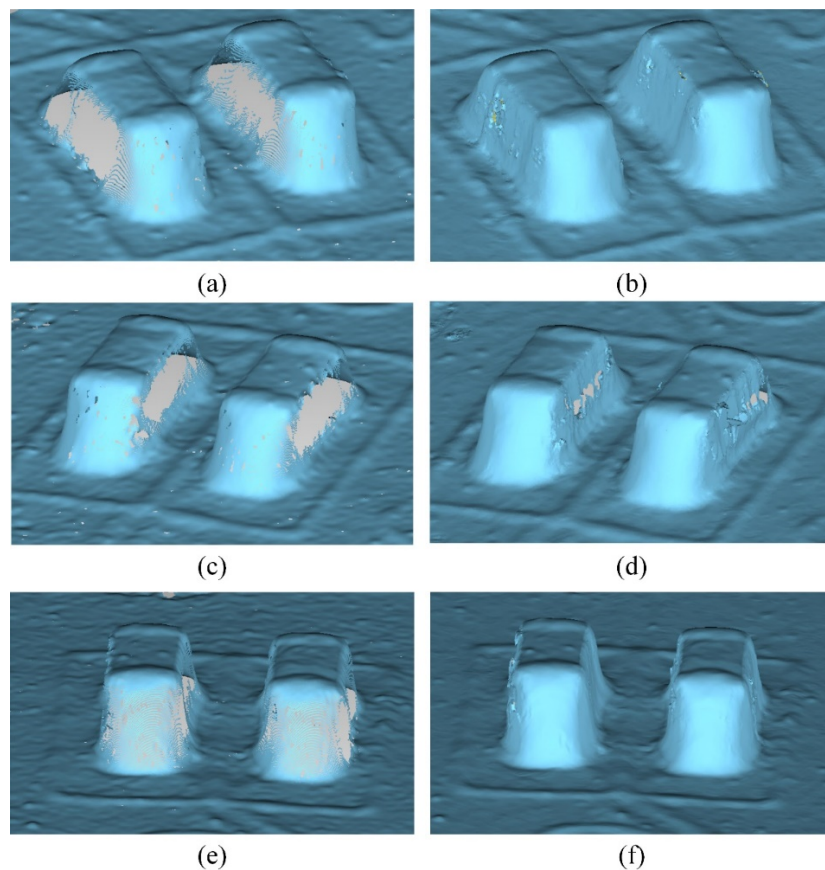


Fig. 13. The range image of surface mount components. (a), (c), (e) Views from different azimuth angles of the range image from single FP-3DM branch. (b), (d), (f) Views from different azimuth angles of the range image from MVFP-3DM.

#### 4. Conclusion

The multi-view fringe projection 3D microscopy (MVFP-3DM) is presented in this paper. The Scheimpflug condition is introduced to make full use of the limited DOF of microscopic imaging. Meanwhile four FP-3DM branches are deployed to improve the performance of micro 3D shape measurement. The general imaging model, which is independent of exact optical layout, is employed to describe the system. In system calibration, to avoid the side effect resulting from out of focus, the edge of binary fringe is used to locate the benchmark. Benefited from the multi-view framework, a group of experiments prove that the proposed MVFP-3DM system has extended measurable range in depth, improved precision in 3D reconstruction and reduced occlusion.

#### Acknowledgments

This work is supported by the National Key R&D Program of China (No.2017YFF0106401). The financial supports from the Natural Science Foundation of China (NSFC) under the grant 61405122 and 61377017 and that from the Sino-German Center for Research Promotion (SGCRP) under the grant GZ 760 are also gratefully acknowledged. This work is also supported by the Key Laboratory of Optoelectronic Devices and Systems of Ministry of Education and Guangdong Province (GD201608).